Particles II

Access the latest eBook →

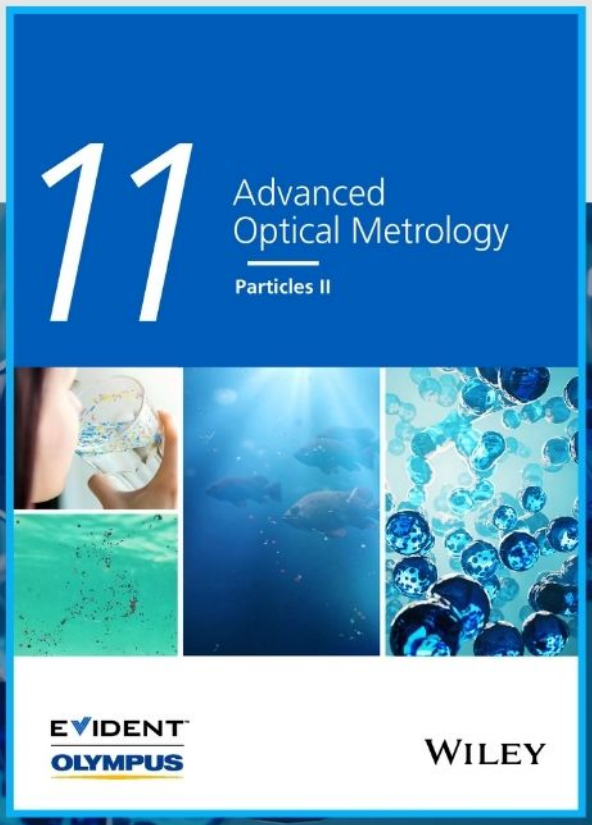

Impact on Biological Systems and the Environment

This eBook is dedicated to the research of Professor David Wertheim.
In collaboration with various groups, Professor Wertheim uses confocal microscopy to analyse the impact of different types of particles on human health and the environment, with a focus on human health-hazardous particles detected with solid-state nuclear track detectors (SSNTD). Download for free, today.

EVIDENT
OLYMPUS

WILEY

ADVANCED MATERIALS
www.advmat.de

A Generalized Method for High-Speed Fluorination of Metal Oxides by Spark Plasma Sintering Yields Ta_3O_7F and TaO_2F with High Photocatalytic Activity for Oxygen Evolution from Water

Martin Alexander Lange, Ibrahim Khan, Phil Opitz, Jens Hartmann, Muhammad Ashraf, Ahsanulhaq Qurashi, Leon Prädel, Martin Panthöfer, Antje Cossmer, Jens Pfeifer, Fabian Simon, Marcus von der Au, Björn Meermann, Mihail Mondeshki, Muhammad Nawaz Tahir, and Wolfgang Tremel**

A general method to carry out the fluorination of metal oxides with poly(tetrafluoroethylene) (PTFE, Teflon) waste by spark plasma sintering (SPS) on a minute scale with Teflon is reported. The potential of this new approach is highlighted by the following results. i) The tantalum oxyfluorides Ta_3O_7F and TaO_2F are obtained from plastic scrap without using toxic or caustic chemicals for fluorination. ii) Short reaction times (minutes rather than days) reduce the process time the energy costs by almost three orders of magnitude. iii) The oxyfluorides Ta_3O_7F and TaO_2F are produced in gram amounts of nanoparticles. Their synthesis can be upscaled to the kg range with industrial sintering equipment. iv) SPS processing changes the catalytic properties: while conventionally prepared Ta_3O_7F and TaO_2F show little catalytic activity, SPS-prepared Ta_3O_7F and TaO_2F exhibit high activity for photocatalytic oxygen evolution, reaching photoconversion efficiencies up to 24.7% and applied bias to photoconversion values of 0.86%. This study shows that the materials properties are dictated by the processing which poses new challenges to understand and predict the underlying factors.

The search for clean, low-cost, and renewable energy sources is one important challenge of modern industrial societies.[1] Hydrogen generated by photochemistry has been identified as a promising energy carrier with high energy density and zero CO_2 emission while being environmentally clean.[2,3] To set up a light-driven and hydrogen based economy an exploration of new materials for eco-friendly, economically viable, stable, and efficient photocatalysts is needed.[4] Noble metals like platinum, iridium, and ruthenium are efficient catalysts for the electrolysis of water, but their scarcity and high-costs limit large-scale technological use.[5] The development of cheap and active catalysts with long-term stability for the hydrogen or oxygen evolution reaction in standard electrolytes is an important goal.

M. A. Lange, P. Opitz, J. Hartmann, Dr. M. Panthöfer, Dr. M. Mondeshki, Prof. W. Tremel
Chemistry Department
Johannes Gutenberg-Universität
Duesbergweg 10-14, Mainz D-55128, Germany
E-mail: tremel@uni-mainz.de

The ORCID identification number(s) for the author(s) of this article can be found under https://doi.org/10.1002/adma.202007434.

[+]Present address: Department of Chemistry, Main Campus, Khalifa University, Abu Dhabi 127788, UAE

DOI: 10.1002/adma.202007434

Dr. I. Khan
Center of Integrative Petroleum Research
King Fahd University of Petroleum & Minerals
Dhahran 31261, Saudi Arabia

Dr. I. Khan, Dr. A. Qurashi[+]
Center of Excellence in Nanotechnology
King Fahd University of Petroleum & Minerals
Dhahran 31262, Saudi Arabia

M. Ashraf, Dr. M. N. Tahir
Chemistry Department
King Fahd University of Petroleum & Minerals (KFUPM)
P.O. Box 5048, Dharan 31261, Kingdom of Saudi Arabia
E-mail: muhammad.tahir@kfupm.edu.sa

L. Prädel
Max Planck Institute for Polymer Research
Ackermannweg 10, 55128 Mainz, Germany

A. Cossmer, J. Pfeifer, F. Simon, M. von der Au, Dr. B. Meermann
Federal Institute for Materials Research and Testing (BAM)
Division 1.1–Inorganic Trace Analysis
Richard-Willstätter-Straße 11, Berlin D-12489, Germany

Among the established and efficient photocatalysts for water splitting (hydrogen evolution (HER) and oxygen evolution (OER) systems) are TiO_2 and metal-TiO_2 heterostructures,[6,7] α-Fe_2O_3,[8,9] CoO,[10] $BiVO_4$,[11] layered niobates,[12] perovskites,[3] layered metal chalcogenides,[13] metal nitrides,[14] and oxynitrides.[15,16] Recently, metal-free polymeric carbon nitride photocatalysts (e.g., g-C_3N_4)[17] became accessible.

While HER photocatalysts containing precious metals (Pd, Pt) or earth abundant 3d transition metal oxides (e.g., TiO_2,[6,7] Fe_2O_3,[8,9] CoO,[10] spinels[18] or nitrides,[14,17] and oxynitrides of the group 5 metals[19,20] have been in the scientific focus since many years, oxyfluorides of the 4d or 5d transition metals[21–28] received less attention, although they show good stability against photo- or chemical corrosion, are nontoxic, and have suitable bandgaps.[29,30] It has been proposed that the proton acidity in the oxide/hydroxide semiconductors $Nb_3O_7(OH)$ [31] can promote the adsorption of water, CO_2, or organic molecules.[32] $Nb_3O_7(OH)$[31] or Nb_3O_7F[29,30] have been reported as photocatalysts for dye degradation and dye-sensitized solar cells, but the photocatalytic properties of $Nb_3O_7(OH)$[32] and the related niobium or tantalum oxyfluorides toward water splitting reactions are still unexplored.[29,30]

The use of oxyfluorides like Nb_3O_7F[21–28] or TaO_2F[22,24,26,28,33] for photocatalysis is hampered by synthetic and processing difficulties.[34] Their chemical synthesis requires fluorine gas, reactive fluorides, or hydrogen fluoride as toxic and corrosive sources of fluorine that make special equipment and techniques for handling indispensable.[26,33,35] The standard route to NbO_2F is based on the reaction of Nb_2O_5 with concentrated HF solution in water.[26] Evaporation to dryness and heating at elevated temperatures leads to the formation of NbO_2F.[21,26] The product composition depends on the sample history, and HF adduct intermediates and mixed hydroxylated/fluorinated products $Nb_{1-x}O_{2-5x}(OH,F)_{1+5x}$ with OH defects and metal vacancies are formed.[26] Efficient fluorination can be performed with HF only under extreme conditions in sealed gold ampoules.[36] High-temperature reactions using binary fluorides as fluorinating agents have limitations due to the high stability of the starting compounds.[35,36]

To address these weaknesses, alternative fluorination pathways[37] to oxyfluorides have been pursued. We devised a new approach for the bulk synthesis of tantalum oxyfluorides from tantalum oxide and fluoropolymers (e.g., poly(tetrafluoroethylene) (PTFE, Teflon)) under mild conditions contrasting dramatically with conventional chemical approaches. Using Teflon scrap that does not meet specifications during polymer processing as feedstock for fluorination is an elegant way of polymer waste disposal. The oxyfluorides Ta_3O_7F and TaO_2Fwere prepared by spark plasma sintering (SPS),[38,39] an energy efficient method enabling the densification of large samples by low electric current levels. SPS is typically used for fast industrial high-temperature processing (> 1000 °C) of ceramics and alloys.[38,39] It is based on a modified hot-pressing process, where pulsed electric currents (the "spark plasma") are passed directly through the pressing mold and the sample.[38,39] This allows for rapid short heating and cooling, metastable products and also for short process cycles. The energy efficiency and processing speed make SPS meaningful for materials manufacturing in industry (responsible for ≈7% of the primary energy and greenhouse gases in Germany) from an economic and environmental point of view.[38]

Although SPS has opened up new options for sintering materials, applications in solid-state synthesis are rare.[40] Engineering nanoscale interfaces is a requisite for harnessing electrical transport within nanostructured materials, especially for photocatalytic applications. Reactions in electric fields affect the reaction kinetics by suppressing granular growth which alters the nature of the final product.[38,39] The primary effect of current in sintering techniques is Joule heating, but other nonthermal effects may contribute to the solid-state reaction kinetics as well. Therefore, SPS allows making metastable materials that cannot be obtained by conventional chemistry.[41,42] Our approach relies on the chemical stability of fluorinated polymers at room temperature and their relatively low decomposition temperature compared to inorganic solids.[43,44] Ta_3O_7F and TaO_2F were synthesized in a "trash to treasure" approach by reacting Ta_2O_5 with PTFE under SPS conditions. The reactions were complete after a few minutes and led to the formation of Ta_3O_7F and TaO_2F polycrystals with high photocatalytic activity, whereas the activity of the corresponding bulk phases (obtained after days by conventional solid-state reactions) was low. The conceptional advance of this study is the evidence that the microstructure and the metastability of the SPS reactions products affect—and strongly enhance—the materials properties. The practical advance of this new bottom-up approach lies in the combination of the versatility and scalability of SPS preparation for environmentally benign fluorination, the use of PTFE polymer scrap for waste removal and the fast and energy efficient synthesis of valuable photocatalysts.

Ta_3O_7F and TaO_2F were prepared as single-phase reaction products (**Figure 1**A,B) by SPS from Ta_2O_5 and PFTE according to

$$Ta_2O_5 + 1/2n(C_2F_4)_n = 2TaO_2F + CO \quad (1)$$

and

$$3Ta_2O_5 + 1/2n(C_2F_4)_n = 2Ta_3O_7F + CO \quad (2)$$

CO gas is released from the SPS press without carbothermal reduction below 750 °C. In the first step, the starting materials PTFE and Ta_2O_5 were mixed in a planetary ball mill using ethanol as dispersion medium for 6 h prior to the reaction. In the subsequent, pyrometer-controlled step the reactants were heated using the temperature profile shown in Figure 1C. The products typically contained phase mixtures with densities of ≈90% of the calculated theoretical density. Phase pure TaO_2F was obtained at 600 °C. Ta_3O_7F could be synthesized with ≈90% purity (side phase TaO_2F) at 600 °C. SPS synthesis requires a small excess of fluorine for Ta_3O_7F (0.36 or 10% excess, calculated by fluorine in PTFE to tantalum in Ta_2O_5) and a large excess for TaO_2F (≥1.5 or 50% excess). For SPS reactions at temperatures ≥ 650 °C Ta_3O_7F contained less TaO_2F contaminants, but still unreacted Ta_2O_5 (due to thermal loss of gaseous $(C_2F_4)_n$). Therefore, a relatively low pressure (19 MPa) was used for the synthesis, as high pressures lead to losses of PTFE decomposition products. For temperatures above 700 °C subsequently less tantalum oxyfluoride was formed, likely due to thermal loss of gaseous $(C_2F_4)_n$ before the reaction (SPS pressing tools are not closed and the reaction uses dynamic vacuum conditions) and slow thermal decomposition of oxyfluoride product. A table summarizing the phase distribution as a function of the

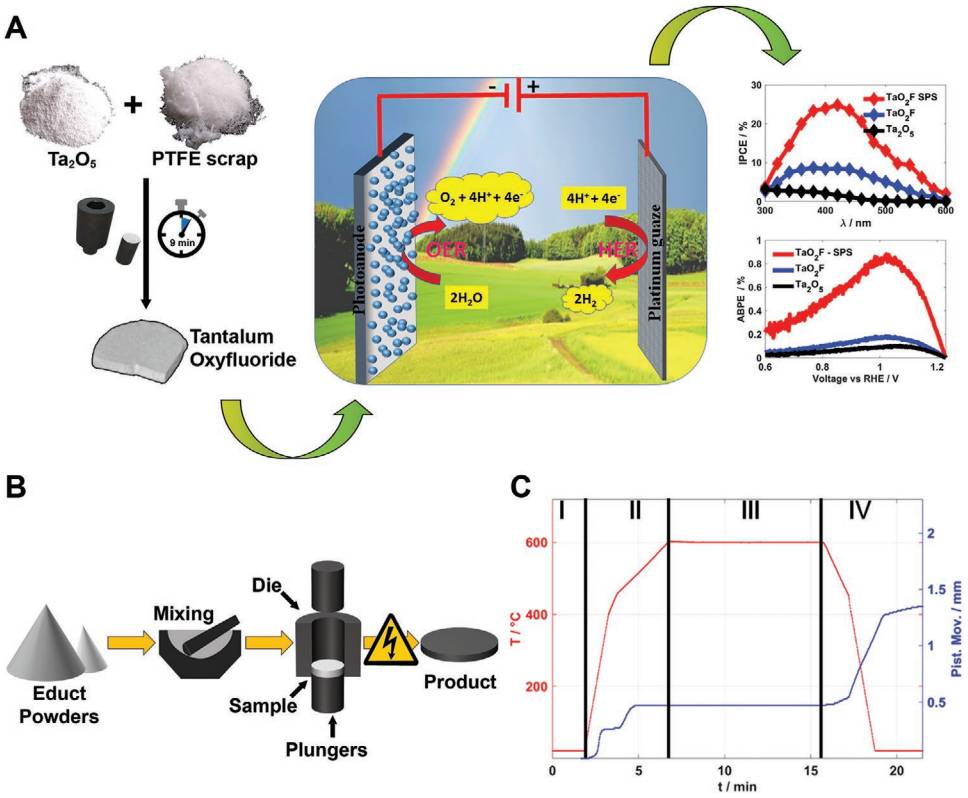

Figure 1. A) General approach to convert Ta_2O_5 and Teflon scrap to tantalum oxyfluoride by SPS in minute intervals and enhanced photocatalytic properties compared to conventionally prepared tantalum oxyfluoride and a Ta_2O_5 reference, indicated by wavelength-dependent incident photon-to-current efficiency (IPCE, upper plot top right) and applied bias to photoconversion (ABPE, lower plot top right). B) Illustration of the SPS synthesis. Precursor materials are mixed by ball milling, then placed in a graphite pressing tool (die and plungers) before transfer into an SPS press. C) Temperature profile (red) and piston movement/densification (blue) during the SPS process. Capital letters indicate different segments for the TaO_2F-synthesis: I Evacuation of reaction chamber and first compression, II start of reaction by heating to 600 with 50 °C min^{-1}, III dwelling at 600 °C for 9 min from and IV sample cooling.

SPS conditions is supplied in the supplementary information (Table S1, Supporting Information). Single-phase Ta_3O_7F could be prepared by conventional ampoule synthesis.

The reaction is assumed to proceed when PTFE undergoes thermolysis above 360 °C.[44] Thermal analysis showed the thermolysis to be complete above 400°. The C_2F_4 monomer is the main decomposition product at 400 °C under vacuum conditions.[44] The complete decomposition of PTFE was confirmed by the absence of PTFE signals in ^{19}F magic-angle-spinning solid-state nuclear magnetic resonance spectroscopy experiments (^{19}F MAS-NMR). Thus, excess PTFE is either completely carbonized or removed in form of volatile decomposition products from the product.

The reaction of Ta_2O_5 with PTFE is likely to occur at the gas–solid interface. Under SPS conditions, monomeric C_2F_4 resulting from the thermal decomposition of PTFE in the carbon die diffuses into the Ta_2O_5 pellet. The fluorination mechanism cannot be analyzed in detail because i) the state of C_2F_4 under the reaction conditions (19 MPa, 600 °C) is unknown, and ii) follow-up reactions of monomeric C_2F_4 may form carbon or fluorocarbons depending on the reaction temperature and pressure.

Phase analysis of the samples was carried by X-ray powder diffraction and transmission electron microscopy. The experimental F/Ta ratios are 2:1 (for TaO_2F) and 1:2.5 (for Ta_3O_7F). The maximum fluorine content for TaO_2F is comparable to that obtained in conventional reactions at 650 °C in quartz ampoules starting from Ta_2O_5 and PTFE (ratio 1.5:1 for TaO_2F and 1:3 for Ta_3O_7F).[24,25,27,28] However, fluorination in SPS reactions are much faster (9 min compared to 12 h for TaO_2F and 36 h for Ta_3O_7F). The yields by SPS were 2 g after ≈9 min (compared to 0.2 g of TaO_2F after 12 h and 0.8 g of Ta_3O_7F after ≈36 h by conventional high temperature chemistry). The yields by SPS can easily be upscaled to the kg range with appropriate dies.[38]

After cooling/quenching to room temperature, the cylindrical pellets were removed from the die and treated with SiC abrasive paper to clean the surface. The pellets were ground in a mortar, and the resulting powders were used for electron microscopy and physical characterization. Elemental analysis supports the SPS synthesis of Ta_3O_7F and TaO_2F. The total fluorine content in selected products was determined with a high resolution-continuum source-graphite furnace molecular absorption spectrometer (HR-CS-GFMAS).

The X-ray diffraction (XRD) patterns of TaO_2F (ReO_3 structure type)[22,26,33] and Ta_3O_7F (U_3O_8 structure type)[21,23] (**Figure 2**A,B; and Figure S1, Supporting Information) could be indexed based on cubic (space group: $Pm\bar{3}m$) and orthorhombic (space group: *Cmmm*) unit cells, respectively. Crystallographic details and essential results of the Rietveld refinements for Ta_3O_7F and TaO_2F are compiled in Table S2 (Supporting Information). The powder diffractograms of the SPS-prepared samples show

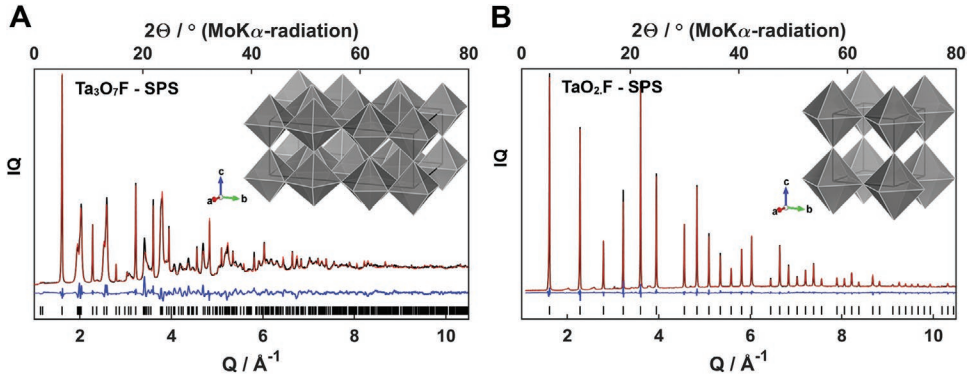

Figure 2. Structural characterization of SPS-prepared Ta_3O_7F and TaO_2F by powder X-ray diffraction. A) Rietveld refinement of SPS-prepared Ta_3O_7F (red line) using X-ray powder data (88% Ta_3O_7F, 12% TaO_2F). B) Rietveld refinement of SPS-prepared TaO_2F (red line) using X-ray powder data. Experimental data: crosses, calculated curve after refinement: continuous line. The tick marks correspond to the Bragg reflections of the cubic and orthorhombic structures. The continuous blue curve under the tick marks represents the difference between the experimental data and the calculated curve. The insets show a polyhedral representation of the crystal structures.

strong anisotropic peak broadening (in comparison to those prepared by conventional chemistry). To achieve satisfactory Rietveld refinements strain parameters based on the Stephens broadening model[45] were applied.

The samples obtained from both, SPS and conventional reactions are phase pure (with minor contamination of TaO_2F for Ta_3O_7F and vice versa). SPS synthesis prevents the formation of mixed hydroxylated/fluorinated products such as $Nb_3O_7(OH)$ completely.[31,32] It is difficult to determine the positions of oxygen and fluorine accurately from XRD data because the scattering contributions of the O and F atoms are almost indistinguishable. Therefore, the analytical F content was determined by HR-CS-GFMAS. This highly specific fluorine analysis is based on the molecular absorption after in situ formation of a diatomic molecule (e.g., "CaF" in the gas phase) in a graphite furnace. Direct fluorine analysis was carried out with a slurry technique.[48] **Table 1** compares the expected fluorine to tantalum ratio (determined by the molecular formula and the phase composition derived from the Rietveld refinements) and by the S experimentally determined fluorine and tantalum concentrations (from HR-CS-GFMA) together with the fluorine to tantalum ratio. The expected fluorine content for both SPS prepared samples (μg kg^{-1}) is higher than the experimentally determined one. While the discrepancy for TaO_2F lies within the experimental error, the deviation for Ta_3O_7F is higher. Possible reasons for this discrepancy could be incomplete sample digestion or the presence of vacancies (as shown by MAS NMR) or the presence of −OH instead of fluorine in the structure. pH-dependent zeta potential measurements show the presence of −OH groups (Table S3, Supporting Information), as confirmed by XPS spectroscopy (Figure 5).

(HR)TEM analysis confirmed Ta_3O_7F and TaO_2F (obtained by SPS at 600 °C) to consist of crystallites in the size range of 10–50 nm, agglomerated and melted together to larger polycrystalline particles in a broad size range between ten and several hundreds of nm (**Figure 3**A,B). Samples obtained by conventional high temperature chemistry at 600 °C (Figure 3C,D) were polycrystalline with larger particle sizes >100 nm and with larger crystalline areas, rarely below 50 nm. N_2 sorption isotherms of SPS-prepared materials showed Brunauer–Emmett–Teller (BET) specific surface areas of 10.28 m^2 g^{-1} (Ta_3O_7F) and 14.20 m^2 g^{-1} (TaO_2F). In contrast, materials produced by conventional ampoule reactions exhibited smaller BET surface areas of 6.18 m^2 g^{-1} (Ta_3O_7F) and 6.82 m^2 g^{-1} (TaO_2F) which confirms the presence of more small particles (<50 nm) and generally smaller polycrystallites for SPS-prepared samples. Particles prepared by SPS had rougher surfaces, while their conventional counterparts had sharp edges. The difference in particle size and BET surface is attributed to the much shorter reaction time (few minutes), a known consequence of SPS processing.[38,39] Line defects and stepped surfaces with layer-like appearance were present for all samples (Figure 3; and Figure S2, Supporting Information), but the SPS samples showed more and more irregular steps, smaller crystallites and more grain boundaries than their conventional counterparts, as confirmed by SEM (Figure S3, Supporting Information). The surface area of SPS samples is approximately two times larger and the number of grain boundaries much higher.

The local structure of SPS-prepared Ta_3O_7F and TaO_2F was probed with total-scattering data via X-ray diffraction, collected at the Diamond beamline ID 15-1. The reduced structure function F(Q) and the pair distribution function (PDF) D(r)

Table 1. Experimental and theoretical fluorine concentration and degree of fluorination determined by HR-CS-GFMAS.

SPS sample	Fluorine concentration via HR-CS-GFMAS [g kg^{-1} ± sd]	Tantalum concentration via HR-CS-GFMAS [g kg^{-1}]	Determined F:Ta ratio (expected values)
Ta_3O_7F (87%) + TaO_2F (13%)	28.4 ± 3.2[a)]	788 ± 14	0.34 ± 0.04:1 (0.41:1)
TaO_2F (95%)	69.5 ± 4.8[a)]	747 ± 29	0.89 ± 0.08:1 (0.97:1)

[a)] $n = 4$.

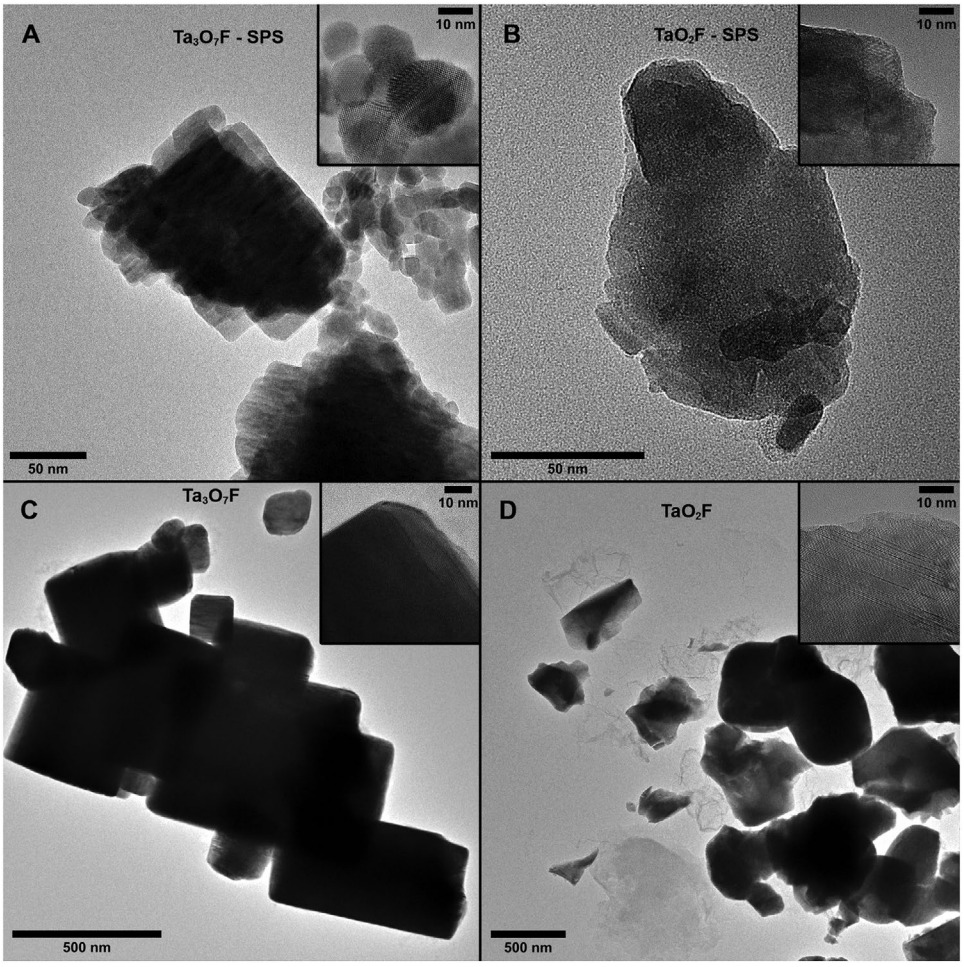

Figure 3. Microstructure of Ta_3O_7F and TaO_2F prepared by SPS and conventional solid-state chemistry. A–D) (HR)TEM images of Ta_3O_7F and TaO_2F prepared by SPS (A,B) and conventional chemistry (C,D). The insets show individual particles in high resolution.

were extracted with the program *GUDRUN4*.[46] We applied the reverse Monte Carlo (RMC) method to obtain structural models for the materials using the software *RMCprofile*.[47] **Figure 4**B shows the F(Q) of the SPS-prepared TaO_2F and the corresponding best RMC fit using the structure of the crystalline phase as the initial model. The resulting model, displayed in Figure 4A, confirms the presence of local distortions and a very high amount of strain in SPS-prepared TaO_2F. Figure 4C shows the pair distribution function $D(r)$ calculated using the experimental total scattering data in comparison to the simulated PDF of crystalline TaO_2F. The peaks of the experimental PDF are much broader and less resolved, which further

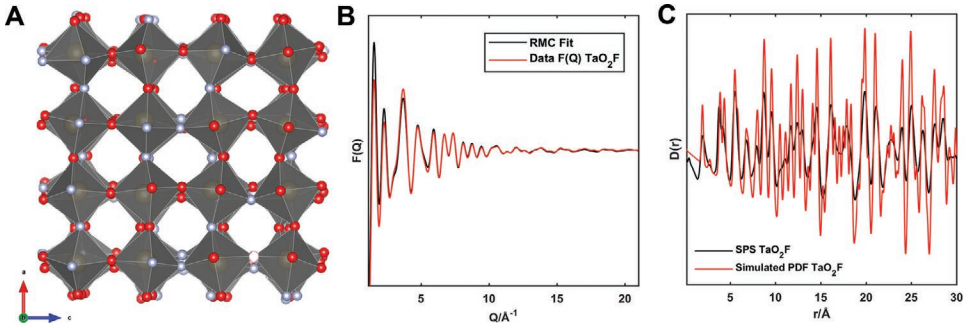

Figure 4. Local structure of SPS-prepared TaO_2F by total scattering. A) Section of the reverse Monte Carlo (RMC) model of SPS prepared TaO_2F obtained from total-scattering data. B) Reduced structure function F(Q) and the corresponding RMC fit and C) pair distribution function (PDF) D(r) in comparison to the simulated PDF function of TaO_2F.

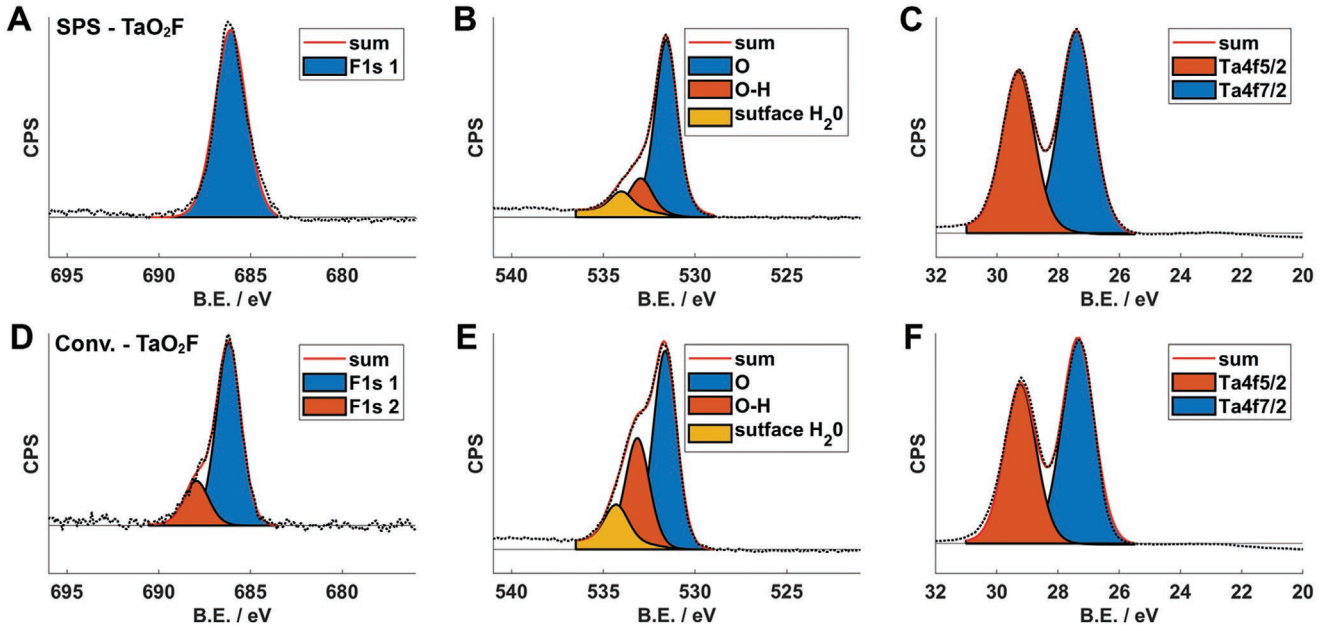

Figure 5. Electronic and surface structure of Ta_3O_7F and TaO_2F prepared by SPS and conventional solid-state chemistry. A–F) XPS spectra (with F, O, and Ta subspectra in (A,D), (B,E), and (C,F)) of TaO_2F, prepared by SPS (A–C) and conventional ampoule chemistry (D–F) with fitted signals for the respective environments.

supports the presence of disorder and strain, i.e., randomly tilted $Ta(O/F)_6$ octahedra lead to a broader bond distance distribution (Figure 4A,C). Furthermore, the PDF of the cubic phase shows significantly more disorder than the PDF of the orthorhombic phase (Figure S4, Supporting Information). This illustrates that the SPS processing leads to local nonequilibrium configurations and therefore metastable structures. This is in agreement with the ^{19}F-MAS NMR results, which show that close fluorine contacts occur more often in SPS prepared than in conventionally prepared material and leads to a less equilibrated atom distribution (Table S5 and Figure S8, Supporting Information).[26,33] All signals are very broad, which is an additional indicator of strong local disorder in SPS-prepared samples.

The bandgap energy (E_g) of a photocatalyst is essential for application in light-driven processes like photocatalytic water splitting reactions. The electronic structures of bulk Ta_3O_7F and TaO_2F, computed with the aid of density functional theory (DFT), are available through the materials genome project.[49] As expected, the conduction bands of both compounds contain mostly Ta 5d contributions, while their valence bands are made up of Ta 6p, O 2p, and F 2p contributions. The computed bandgaps E_g are 2.22 eV for Ta_3O_7F and 2.05 eV for TaO_2F, compared to 3.83 eV for orthorhombic β-Ta_2O_5, [50] a well-known wide band semiconductor.[49] These values show that the differences in E_g between Ta_3O_7F, TaO_2F, and β-Ta_2O_5 are determined by the differences in chemical composition and crystal structure. The computed bandgaps are significantly smaller than the experimental values of 4.03, 4.10, and 4.23 eV (for Ta_3O_7F, TaO_2F, and β-Ta_2O_5; and Figure S5, Supporting Information), which shows the well-known underestimation of the bandgap by standard DFT.[51]

Figure 5A–F shows the F, O, and Ta regions of the XPS spectra of TaO_2F synthesized by SPS (Figure 5A–C) and conventional ampoule chemistry (Figure 5D–F). The XPS survey spectra (Figure S6, Supporting Information) confirm the presence of the elements Ta, O, and F. In Figure 5A,D, the signals centered at 27 and 29 eV are assigned to the Ta 4f 7/2 and Ta 4f 5/2 orbitals, respectively, revealing the oxidation state of 5+ for Ta in TaO_2F. The XPS spectra of the F 1s core electrons (Figure 5C,F) show a signal centered at 686 eV with a less intense additional signal at 688 eV, originating from Ta–F and C–F (remnants of PTFE in conventional ampoule chemistry) bonds on the surface of TaO_2F. The O 1s areas in Figure 5B,E show two signals at 531.5, 533 eV, which correspond to lattice O, surface hydroxyl groups and surface water, respectively. Conventionally prepared TaO_2F shows significantly less surface fluorine compared to the SPS-prepared TaO_2F (Table S4, Supporting Information) (ratio F/O conventional = 1:10, ratio F/O SPS 1:5 to 1:3).

The optical properties of as-prepared Ta_3O_7F and TaO_2F (by SPS and conventional ampoule chemistry) and Ta_2O_5 were determined between 200 and 800 nm by optical UV–vis spectroscopy (Figure S5F, Supporting Information) and compared with the reported and measured optical bandgaps for β-Ta_2O_5. The spectra display absorption edges at ≈300 nm, corresponding to estimated electronic energy bandgap values of 4.03 eV and 4.10 (4.09 and 4.08 eV) for Ta_3O_7F and TaO_2F prepared by SPS (conventional ampoule chemistry) while the determined band-value of β-Ta_2O_5 is 4.23 eV. The indirect bandgaps were determined from the Kubelka–Munk function (Figure S5, Supporting Information) by plotting $(Fh\nu)^{1/2}$ as a function of photon energy ($h\nu$), where F is the normalized Kubelka–Munk function of the diffuse reflectance R (from panel A) (intercept at energy axis).[52] SPS-prepared samples, and especially cubic TaO_2F compared to orthorhombic Ta_3O_7F, clearly show a higher absorption at 2–4 eV, which corresponds to the wavelengths of the light source used in our photoelectric measurements. In addition, the onset of the absorption edges and flat bands (Figure S5F, Supporting Information) of Ta_3O_7F and TaO_2F are shifted to smaller wavelengths compared to β-Ta_2O_5.

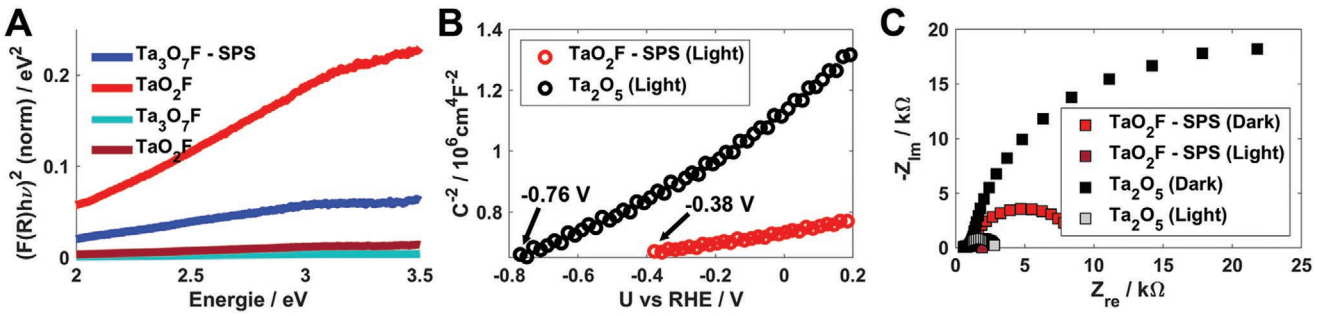

Figure 6. Bandgap, band edge positions, and charge carrier concentrations of Ta_3O_7F and TaO_2F prepared by SPS and conventional solid-state chemistry. A) Low-energy region of Kubelka–Munk Plot of Ta_3O_7F (blue line) and TaO_2F (red line) prepared by SPS (solid lines) and conventional ampoule chemistry (dashed lines). B) Mott–Schottky plot, and C) EIS Nyquist plot spectra under illumination.

Surface states or the morphology of nanostructured materials can affect the band-edge positions.[53] To obtain absolute band-edge positions with respect to water redox potentials we determined the flat-band potentials [54,55] of SPS-prepared TaO_2F by plotting $1/C^2$ as a function of electrochemical potentials, where the capacitance C was obtained from impedance measurements (**Figure 6**B,C). The Mott–Schottky analysis was performed at 1000 Hz frequency. A significant difference in the flat band potentials between Ta_2O_5 and SPS-prepared TaO_2F was observed, the flat band positions (–0.38 V vs RHE for TaO_2F-SPS) allowing for a lower water oxidation potential and enhanced photocurrent. This anodic shift for the flat band potential of the TaO_2F-SPS sample to less negative potential (–0.38 V) from more negative potential (–0.76 V, for Ta_2O_5) photoanodes shows the enhancement in the charge densities (charge carrier concentration). Lower energy is required to knock more electrons, thereby creating more holes for water oxidation.[56–61]

Thus, the high photoelectrochemical (PEC) activity of SPS-prepared TaO_2F is associated with a lowering of the flat-band potential of TaO_2F nanocrystals by ≈0.5 V. The shift of the flat band potentials as evident from the Mott–Schottky plots appears to be related to a reorientation of valence and conductance bands (the bandgap is slightly reduced) upon fluorine addition. New band positions are adopted as confirmed from theoretical calculations of the optical band positions. The calculation method and optical band positions are provided Table S6 and Figure S9 (Supporting Information). The positive slope of the Mott–Schottky plot indicates that TaO_2F is an n-type semiconductor (possibly related to an incomplete O/F substitution).

Ta_3O_7F and TaO_2F synthesized by SPS and conventional ampoule chemistry showed water splitting activity under simulated 1-sun light in photoelectrochemical cells. **Figure 7** provides the PEC results in terms of photocurrent-voltage (*I–V*), stability curve and periodic chopped photocurrent-time (*I–t*) plots. Figure 7A shows the comparative *I–V* response obtained from linear sweep voltammetry (LSV) of Ta_2O_5, and the tantalum oxyfluorides, Ta_3O_7F and TaO_2F (prepared by SPS and conventional chemistry), under continuous irradiation with light. Ta_3O_7F and TaO_2F prepared by SPS showed a good photoresponse behavior with large values of the photocurrent density, i.e., 0.31 and 0.72 mA cm^{-2} at 1.23 V versus RHE for Ta_3O_7F-SPS and TaO_2F-SPS, respectively. In contrast, Ta_3O_7F and TaO_2F, prepared by conventional ampoule chemistry, showed a lower photoresponse with a photocurrent density reaching only 0.17 and 0.13 mA cm^{-2} 1.23 V versus RHE (the minimum threshold voltage for water splitting). The Ta_2O_5 photoanode showed a very small photoresponse under simulated light at voltage 1.23 V versus RHE, which is related to the UV part of the optical spectrum.

TaO_2F-SPS showed a higher photoresponse than Ta_3O_7F-SPS. The orbital overlap in the ReO_3-type structure with Ta-O(F)-Ta bond angles close to 180° [33,62] facilitates charge transfer and charge carrier transport, thereby improving the photocatalytic activity. XPS (Figure 5; and Figure S6 and Table S4, Supporting Information) shows that the overall F atom surface density in TaO_2F-SPS is higher than for Ta_3O_7F-SPS (in agreement with the composition). This improves the efficiency of photocurrent generation. Ta_2O_5, Ta_3O_7F, and TaO_2F photoanodes showed low dark currents (Figure 7B). Another striking effect of the tantalum oxyfluorides is the cathodic shift of the overpotential of the TaO_2F-SPS photoanode to a minimum value of ≈0.55 V versus RHE, which reached to saturation at 1.16 V versus RHE. We achieved a maximum photocurrent density of 0.31 and 0.72 mA cm^{-2} at 1.23 V versus RHE for photoanodes with SPS-prepared Ta_3O_7F and TaO_2F, respectively. In contrast, Ta_3O_7F, TaO_2F, and Ta_2O_5 prepared by conventional ampoule chemistry showed photocurrent values of 0.17, 0.13, and 0.12 mA cm^{-2}, respectively. The photocurrent for TaO_2F at 1.23 V versus RHE enhanced by a factor of six compared to a Ta_2O_5 photoanode (0.12 mA cm^{-2} at 1.23 V versus RHE), the value being roughly comparable with those of hematite (α-Fe_2O_3, 0.45 mA cm^{-2}),[63] pristine CoO_x (≈0.7 mA cm^{-2}) [64] or pristine $BiVO_4$ (1.2 mA cm^{-2} at 1.23 V versus RHE) and pristine $BiVO_4$ photoanodes.[11]

FTa_3O_7F-SPS and TaO_2F-SPS photoanodes were stable for 2 h under continuous light illumination Figure 7C, and TaO_2F showed a better photostability than Ta_3O_7F indicating low photocharge recombination and high charge transfer efficiency. The better photostability of TaO_2F may be attributed to its crystal structure, because TaO_2F is the thermodynamically stable oxyfluoride, whereas Ta_3O_7F is an intermediate during TaO_2F formation. The photocurrent of SPS-prepared Ta_3O_7F started to decay and collapsed after ≈1.5 h, which might be attributed to the recombination of photoexcitons. We also demonstrated the periodic photocurrent generation capacities of Ta_2O_5 and SPS-prepared TaO_2F photoanodes by applying transient irradiation at regular intervals of ≈20 s. Figure 7D shows a consistent decrease and increase of the photocurrent under regular chopped light conditions. The periodic photoresponse was still stable after 10 cycles. To exclude any electrochemical

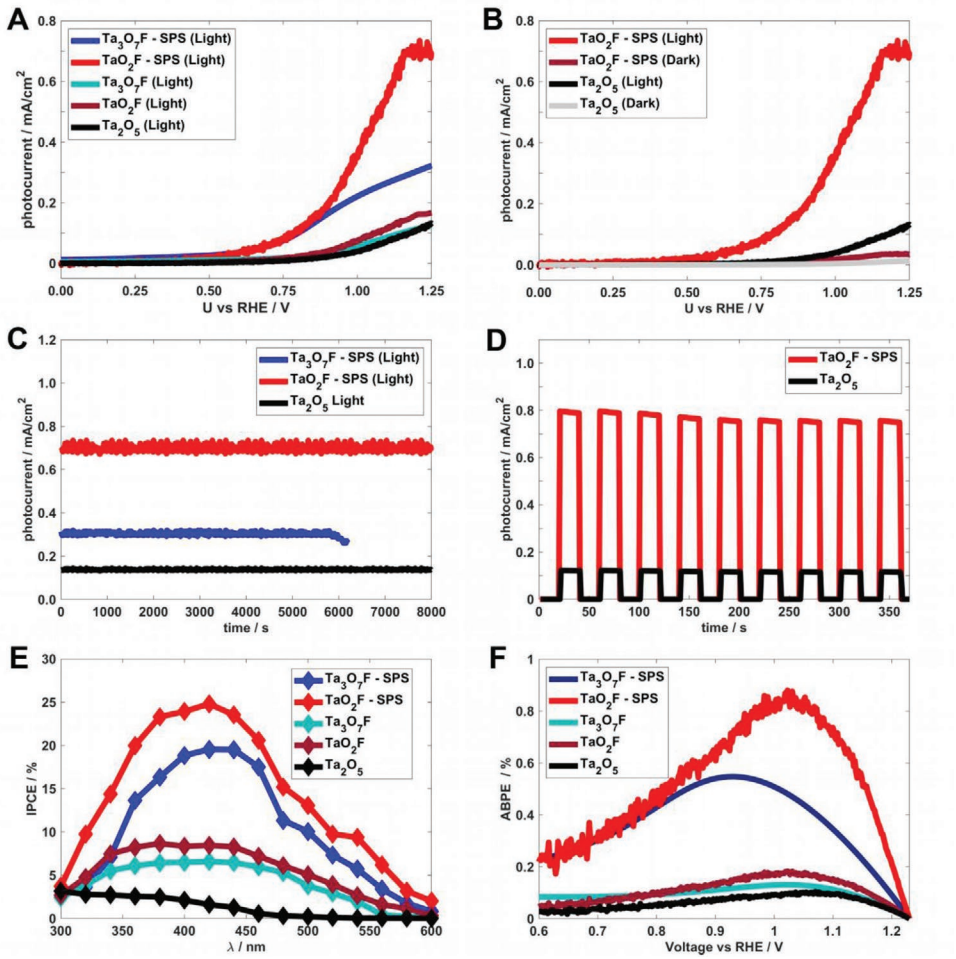

Figure 7. PEC measurements for Ta_2O_5 and the tantalum oxyfluorides, prepared by SPS and conventional ampoules chemistry. A,B) Linear sweep voltammograms under light and dark conditions, C) *I–t* photostability curve under continuous luminescence at 1.23 V versus RHE, and D) amperometric *I–t* curves at an applied potential of 1.23 V versus RHE with 20 s ON/OFF cycle. E) Incident photon-to-current efficiencies, IPCE (%) and F) applied bias to photoconversion ABPE (%) for Ta_2O_5, Ta_3O_7F (SPS-prepared and conventional synthesis) and TaO_2F (SPS-prepared and conventional synthesis).

contribution for water oxidation in this voltage range, we performed an electrochemical analysis (LSV) of freshly prepared photoanodes. Even at 2.00 V versus RHE, no significant contribution from electrochemical response was detected (Figure S10, Supporting Information).

The wavelength-dependent incident photon-to-current efficiency (IPCE) was calculated according to Equation (3)

$$\mathrm{IPCE}(\%) = \frac{1240 \times I_{\mathrm{photon}}}{\lambda \times P_{\mathrm{incident\,light}}} \tag{3}$$

where I_{photon}, λ, and $P_{\mathrm{incident\,light}}$ indicate the photocurrent (mA), the wavelength of the incident light (nm), and the incident irradiating power at the specific wavelength (mW). A Xe lamp fitted with band-pass monochromatic irradiation filters (central wavelengths: 400–600 nm with 20 nm in each pass) was used to measure the IPCE (%) dependence at each value. The monochromatic incident light was quantified by Equation (3) and plotted as a function of wavelength (λ) at 1.23 V versus RHE (Figure 7E). The % IPCE values for SPS-prepared Ta_3O_7F and TaO_2F are substantially higher than that for Ta_2O_5. Figure 7E shows that the Ta_2O_5 photoanode utilized only 3.1% of the incident light compared to Ta_3O_7F and TaO_2F. The comparative % IPCE values (**Table 2**) show the highest photoconversion values for Ta_3O_7F-SPS and TaO_2F-SPS, i.e., tantalum oxyfluoride photoanodes exhibit a strongly enhanced light-absorbing and utilization capacity. Ta_3O_7F-SPS and TaO_2F-SPS

Table 2. Comparison of photochemical parameters and their effect on PEC performance of Ta_3O_7F and TaO_2F photoanodes.

Photoanode	Photocurrent density at 1.23 V vs RHE [mA cm^{-2}]	IPCE [%] at λ nm	ABPE [%] values at potential [V vs RHE]
Ta_3O_7F – SPS	0.33	19.4% at 421 nm	0.55% at 0.93 V
TaO_2F – SPS	0.72	24.7% at 415 nm	0.86% at 1.01 V
Ta_3O_7F	0.11	6.7% at 374 nm	0.13% at 1.04 V
TaO_2F	0.17	8.7% at 384 nm	0.19% at 1.01 V
Ta_2O_5	0.13	3.1% at 300 nm	0.102% at 1.09 V

showed photoconversion efficiencies of 19.4% and 24.7%, the highest values reported so far for such materials. Importantly, a sufficient absorption occurs in the visible range of the solar spectrum (400–700 nm).

We transformed the *I*–*V* data (recorded by a three-electrode system) to % applied bias to photoconversion (% ABPE) efficiency according to Equation (4)[65,66]

$$\mathrm{ABPE}(\%) = \frac{J_{\mathrm{ph}}\left(1.23 - \left|V_{\mathrm{app}}\right|\right)}{P_{\mathrm{light}}} \times 100 \tag{4}$$

where J_{ph} is the photocurrent density (mA cm^{-2}), V_{app} is the applied potential versus RHE, and P_{light} is the power density of illumination (100 mW cm^{-2}). The results are shown in Figure 7F. The ABPE for the TaO_2F-SPS photoelectrode was up to 0.86% at 1.01 V versus RHE, which is about eight times higher than the corresponding value for a Ta_2O_5 electrode and higher than, or comparable to the values for hematite (0.24%)[57] and pristine $BiVO_4$ (≈1%).[11] Similarly, a SPS-prepared Ta_3O_7F photoelectrode also showed a good ABPE value of 0.55% at 0.93 V versus RHE. In contrast, Ta_3O_7F and TaO_2F prepared by conventional ampoule chemistry showed much lower ABPE values of 0.13% and 0.19%, respectively. These results show the importance of materials processing during synthesis for the light-induced characteristics of the material.

Interfacial charge transfer, a critical factor to test the PEC efficiency of photocatalysts, was determined by electronic impedance spectroscopy (EIS) under simulated solar condition. Measurements were conducted by sweeping a DC voltage across the working electrode. Nyquist plots (real vs imaginary) with representative impedance values for Ta_2O_5, Ta_3O_7F-SPS, and TaO_2F-SPS are shown in Figure 7C. The impedance is indicative of interfacial phenomena operative near the electrode surface. As expected, the charge transfers kinetics in TaO_2F-SPS is more dominant compared to Ta_2O_5, which explains the lower resistance curve in Figure 6C. The higher electrical conductivity is attributed to an increased exciton density generated by photons of lower energy.

Thus, F/O replacement appears to be a crucial factor for the enhanced photoelectrical efficiency of Ta_3O_7F and TaO_2F. It leads to a "band realignment" and leads (for TaO_2F) to structural changes that facilitate charge transfer and carrier separation. A reduced charge carrier recombination rate that enhances the photocatalytic activity has been reported in fluorine-doped oxides and attributed to the presence of additional energy levels and alternative pathways that enhance exciton life times.[67–69]

Importantly, SPS preparation prevents the growth of large crystallites, generates a larger BET surface, more grain boundaries and thus more active surface sites. In addition, SPS reduces surface passivation due to surface O—H with increasing fluoride content. This is supported by the XPS results, which are compatible with the presence of surface F-atoms and defect formation, while the Mott–Schottky analysis (Figure 6B,C) revealed a band repositioning of the bands for tantalum oxyfluorides.

In summary, we demonstrated a very fast, energy saving, and environmentally benign synthesis for tantalum oxyfluoride photocatalysts by SPS starting from PTFE scrap as solid, nontoxic and abundant source of fluorine. SPS processing reduces reaction times to the order of minutes rather than days, which reduce process times and the energy costs by several orders of magnitude. Local strain and atom disorder due to the SPS-processing makes TaO_2F an active photocatalysts with a ReO_3-type F/O disordered substructure, which shows, even in the absence of cocatalysts, an excellent photocatalytic activity for oxygen evolution, reaching photoconversion efficiencies up to 24.7% and applied bias to photoconversion values of 0.86%. In contrast, conventionally prepared TaO_2F shows only moderate photoactivity. Similarly, SPS-prepared Ta_3O_7F exhibits unique electronic properties, endowing it with good electron transfer abilities for photocatalytic oxygen generation. In view of their low charge transfer resistance, the corresponding niobium oxyfluorides may have prospects in photoelectro- or electrochemistry as well. Microstructural changes due to nonequilibrated atom distributions, atom disorder, grain boundaries and thus more active surface sites are generally not considered in electronic structure calculations which are based on equilibrium structures. This study is a proof of concept for the rapid and energy saving production of valuable photocatalysts for water splitting from plastic waste without using toxic or caustic chemicals. It opens new perspectives for the recycling of plastic waste and the search of stable photocatalysts by materials processing.

Supporting Information

Supporting Information is available from the Wiley Online Library or from the author.

Acknowledgements

M.A.L. is recipient of a Carl-Zeiss fellowship. This research was supported by a grant from the Deutsche Forschungsgemeinschaft within the priority program Manipulation of Matter Controlled by Electric and Magnetic Fields: Toward Novel Synthesis and Processing Routes of Inorganic Materials (SPP 1959). The authors thank Diamond Light Source for beamtime (proposal CY23320), and the staff, especially Thomas Forrest, of beamline I15-1 (XPDF) for rapid access measurements.

Open access funding enabled and organized by Projekt DEAL.

Conflict of Interest

The authors declare no conflict of interest.

Data Availability Statement

Research data are not shared.

Keywords

fluorination, oxygen evolution reaction, photocatalysis, spark plasma sintering, tantalum oxyfluorides

Received: October 30, 2020
Revised: December 19, 2020
Published online: April 10, 2021

[1] M. J. Burke, J. J. Stephens, *Energy Res. Social Sci.* **2018**, *35*, 78.
[2] H. B. Gray, *Nat. Chem.* **2009**, *1*, 7.
[3] J. Suntivich, K. J. May, H. A. Gasteiger, J. B. Goodenough, Y. Shao-Horn, *Science* **2011**, *334*, 1383.
[4] I. Staffell, D. Scamman, A. V. Abad, P. Balcombe, P. E. Dodds, P. Ekins, N. Shahd, K. R. Warda, *Energy Environ. Sci.* **2019**, *12*, 463.
[5] I. Roger, M. A. Shipman, M. D. Symes, *Nat. Rev. Chem.* **2017**, *1*, 0003.
[6] J. Schneider, M. Matsuoka, J. Zhang, Y. Horiuchi, M. Anpo, D. W. Bahnemann, *Chem. Rev.* **2014**, *114*, 9919.
[7] F. E. Osterloh, *Chem. Soc. Rev.* **2011**, *42*, 2294.
[8] A. Kay, I. Cesar, M. Grätzel, *J. Am. Chem. Soc.* **2006**, *128*, 15714.
[9] O. Zandi, T. W. Hamann, *Nat. Chem.* **2016**, *8*, 778.
[10] L. Liao, Q. Zhang, Z. Su, Z. Zhao, Y. Wang, Y. Li, X. Li, D. Wei, G. Feng, Q. Yu, X. Cai, J. Zhao, Z. Ren, H. Fang, F. Robles-Hernandez, S. Baldelli, J. Bao, *Nat. Nanotechol.* **2014**, *9*, 69.
[11] T. W. Kim, K.-S. Choi, *Science* **2014**, *343*, 990.
[12] T. Oshima, O. Ishitani, K. Maeda, *Adv. Mater. Interfaces* **2014**, *1*, 1400131.
[13] T. F. Jaramillo, K. P. Jorgensen, J. Bonde, J. H. Nielsen, S. Horch, I. Chorkendorff, *Science* **2007**, *317*, 100.
[14] L. Yuliati, J. H. Yang, X. C. Wang, K. Maeda, T. Takata, M. Antonietti, K. Domen, *J. Mater. Chem.* **2010**, *20*, 4295.
[15] K. Maeda, K. Teramura, D. Lu, T. Takata, N. Saito, Y. Inoue, K. Domen, *Nature* **2006**, *44*, 295.
[16] K. Maeda, D. Lu, K. Domen, *Angew. Chem., Int. Ed.* **2013**, *52*, 6488.
[17] X. C. Wang, K. Maeda, A. Thomas, K. Takanabe, G. Xin, J. M. Carlsson, K. Domen, M. Antonietti, *Nat. Mater.* **2009**, *8*, 76.
[18] L. Reith, K. Lienau, C. A. Triana, S. Siol, G. R. Patzke, *ACS Omega* **2019**, *4*, 15444.
[19] T. Hisatomi, C. Katayama, Y. Moriya, T. Minegishi, M. Katayama, H. Nishiyama, T. Yamadad, K. Domen, *Energy Environ. Sci.* **2013**, *6*, 3595.
[20] C. Pan, T. Takata, M. Nakabayashi, T. Matsumoto, N. Shibata, Y. Ikuhara, K. Domen, *Angew. Chem., Int. Ed.* **2015**, *54*, 2955.
[21] S. Andersson, *Acta Chem. Scand.* **1964**, *18*, 2339.
[22] L. Jahnberg, S. Andersson, *Acta Chem. Scand.* **1967**, *21*, 615.
[23] M. Vlasse, C. Morilliere, J.-P. Chaminade, M. Poucard, *Bull. Mineral.* **1975**, *98*, 325.
[24] D. Hirai, E. Climent-Pascual, R. J. Cava, *Phys. Rev. B* **2011**, *84*, 17451.
[25] S. E. Dutton, D. Hirai, R. J. Cava, *Mat. Res. Bull.* **2012**, *47*, 714.
[26] J. Dabachi, M. Body, C. Galven, F. Boucher, C. Legein, *Inorg. Chem.* **2017**, *56*, 5219.
[27] D. Hirai, O. Sawai, T. Nunoura, Z. Hiro, *J. Fluorine Chem.* **2018**, *209*, 43.
[28] M. A. Lange, Y. Krysiak, J. Hartmann, G. Dewald, G. Cerretti, M. N. Tahir, M. Panthöfer, B. Barton, T. Reich, W. G. Zeier, M. Mondeshki, U. Kolb, W. Tremel, *Adv. Funct. Mater* **2020**, *30*, 1909051.
[29] H. Zhang, Y. Li, Y. Wang, P. Liu, H. Yang, X. Yao, T. An, B. J. Wood, H. Zhao, *J. Mater. Chem. A* **2013**, 1, 6563.
[30] J. Duan, G. Mou, S. Zhang, S. Wang, J. Guan, *J. Mater. Chem. A* **2015**, *3*, 14686.
[31] H. Zhang, H. Wang, P. Liu, S. L. Chou, J. Z. Wang, H. Liu, G. Wang, H. Zhao, *ACS Nano* **2016**, *10*, 507.
[32] M. Mhadeh, V. Hoepfner, E. Larios, K. Liao, J. Jia, M. Jose-Yacaman, G. A. Ozin, *ChemSusChem* **2014**, *7*, 2104.
[33] C. R. Morelock, B. K. Greve, M. Cetinkol, K. W. Chapman, P. J. Chupas, A. P. Wilkinson, *Chem. Mater.* **2013**, *25*, 1900.
[34] A. D. Menard, J. F. Trant, *Nat. Chem.* **2020**, *12*, 17.
[35] E. Kemnitz, J. Noack, *Dalton Trans.* **2015**, *44*, 19411.
[36] W. Sleight, *Inorg. Chem.* **1969**, *8*, 1764.
[37] Y. Kobayashi, M. Tian, M. Eguchi, T. E. Mallouk, *J. Am. Chem. Soc.* **2009**, *131*, 9849.
[38] O. Guillon, C. Elsässer, O. Gutfleisch, J. Janek, S. Korte-Kerzel, D. Raabe, C. A. Volkert, *Mater. Today* **2018**, *21*, 527.
[39] O. Guillon, J. Gonzales-Julian, B. Dargartz, T. Kessel, G. Schierning, J. Räthel, M. Herrmann, C. Sässer, O. Gutfleisch, J. Janek, S. Korte-Kerzel, D. Raabe, C. A. Volkert, *Adv. Eng. Mater.* **2014**, *16*, 830.
[40] C. Recknagel, N. Reinfried, P. Höhn, W. Schnelle, H. Rosner, Y. Grin, A. Leithe-Jasper, *Sci. Techn. Adv. Mat.* **2007**, *8*, 357.
[41] M. Beekman, M. Baitinger, H. Borrmann, W. Schnelle, K. Meier, G. S. Nolas, Y. Grin, *J. Am. Chem. Soc.* **2009**, *131*, 9642.
[42] D. Portehault, V. Maneeratana, C. Candolfi, N. Oeschler, I. Veremchuk, Y. Grin, C. Sanchez, M. Antonietti, *ACS Nano* **2011**, *5*, 9052.
[43] E. E. Lewis, M. A. Taylor, *J. Am. Chem. Soc.* **1947**, *69*, 1968.
[44] B. B. Baker, D. J. Kasprzak, *Polym. Degrad. Stabil.* **1993**, *42*, 181.
[45] P. W. Stephens, *J. Appl. Cryst.* **1999**, *32*, 281.
[46] S. E. McLain, D. T. Bowron, A. C. Hannon, A. K. Soper, *ISIS Facility*, Rutherford Appleton Laboratory, Chilton, Didcot, Oxfordshire, UK.
[47] M. G. Tucker, D. A. Keen, M. T. Dove, A. L. Goodwin, Q. Hui, *J. Phys. Condens. Mater.* **2007**, *19*, 335218.
[48] N. Ozbe, S. Akman, *Food Anal. Methods* **2016**, *9*, 2925.
[49] A. Jain, S. P. Ong, G. Hautier, W. Chen, W. D. Richards, S. Dacek, S. Cholia, D. Gunter, D. Skinner, G. Ceder, K. Persson, *Appl. Phys. Lett. Mater.* **2013**, *1*, 011002.
[50] R. Nashed, W. M. I. Hassan, Y. Ismail, N. K. Allam, *Phys. Chem. Chem. Phys.* **2013**, *15*, 1352.
[51] A. Morales-García, R. Valero, F. Illas, *J. Phys. Chem. C* **2017**, *121*, 18862.
[52] G. Kortüm, *Reflectance Spectroscopy*, Springer, Berlin, Germany **1969**.
[53] S. M. Sze, M. K. Le, *Semiconductor Devices – Physics and Technology*, Wiley, New York **2010**.
[54] A. Hankin, F. E. Bedoya-Lora, J. C. Alexander, A. Regoutz, G. H. Kelsall, *J. Mater. Chem. A* **2019**, *7*, 26162.
[55] C. Lohaus, A. Klein, W. Jaegermann, *Nat. Commun.* **2018**, *9*, 4309.
[56] Y. Zhu, J. Xu, H. Jiang, D. Niu, X. Zhang, S. Hu, *CrytEngComm* **2018**, *20*, 6430.
[57] S. W. LaGasse, P. Dhakras, K. Watanabe, T. Taniguchi, J. U. Lee, *Adv. Mater.* **2019**, *31*, 1901392.
[58] T. Xu, L. Zhang, H. Cheng, Y. Zhu, *Appl. Catal., B* **2011**, *101*, 382.
[59] C. Liu, Y. Qui, F. Wang, Q. Liang, Z. Chen, *Adv. Mater. Interfaces* **2017**, *4*, 1700681.
[60] S. S. Kalanur, *Catalysts* **2019**, *9*, 456.
[61] Z. Zhang, P. Wang, *Energy Environ. Sci.* **2012**, *5*, 6506.
[62] K. Kamali, T. R. Ravindran, T. N. Sairam, *Vibr. Spectr.* **2014**, *71*, 12.
[63] Gurudayal, S. Y. C. , M. H. Kumar, P. S. Bassi, H. L. Seng, J. Barber, L. H. Wong, *ACS Appl. Mater. Interfaces* **2014**, *6*, 5852.
[64] M. Favaro, J. Yang, S. Nappini, E. Magnano, F. M. Toma, E. J. Crumlin, J. Yano, I. D. Sharp, *J. Am. Chem. Soc.* **2017**, *139*, 8960.
[65] Y. Wan, S. K. Karuturi, C. Samundsett, J. Bullock, M. Hettick, D. Yan, J. Peng, P. R. Narangari, S. Mokkapati, H. H. Tan, C. Jagadish, A. Javey, A. Cueva, *ACS Energy Lett.* **2018**, *3*, 125.
[66] T. Hisatomi, J. Kubota, K. Domen, *Chem. Soc. Rev.* **2014**, *43*, 7520.
[67] S. Y. Moon, E. H. Gwag, J. Y. Park, *Energy Technol.* **2018**, *6*, 459.
[68] L. Liu, Z. Mei, Y. Hou, H. Liang, A. Azarov, V. Venkatachalapathy, A. Kuznetsov, X. Du, *Sci. Rep.* **2015**, *5*, 15516.
[69] Y. Zhu, J. Xu, H. Jiang, D. Niu, X. Zhang, S. Hu, *CrystEngComm* **2018**, *20*, 6430.